An examination of the spherical scatterer approximation in aqueous suspensions of sand

Jinyu Sheng and Alex E. Hay
Department of Physics and Newfoundland Institute for Cold Ocean Science, Memorial University of Newfoundland, St. John's, Newfoundland A1B 3X7, Canada

(Received 12 March 1987; accepted for publication 15 September 1987)

The available data for scattered acoustic intensity and attenuation in dilute aqueous suspensions of sand are compared with theory. In theoretical calculations, the scatterer is assumed to be spherical and elastic, or rigid and movable, or rigid and immovable. The rigid movable model provides the best fit to the data. The failure of the elastic model in comparison to the rigid sphere models indicates that resonance excitation does not occur in natural sand grains, probably because of irregularities in shape. The fact that better agreement with experiment is obtained with the rigid movable model than with the rigid immovable model indicates that the inertia of the particles is important. Additional approximate expressions for the form factor and attenuation coefficient have been constructed based on a modified form of the so-called high-pass model introduced by Johnson [J. Acoust. Soc. Am. **61**, 275–277 (1977)]. The modified high-pass model provides a fit to the data that is as good as, or better than, the rigid movable case.

PACS numbers: 43.30.Ft, 43.30.Gv

INTRODUCTION

Interest in the problem of sound propagation in particulate suspensions has developed in part because of the potential of acoustic methods for suspended sediment measurement in aqueous environments. The greatest advantage of this approach over others is that, in principle, quantitative results can be obtained remotely and therefore with minimal disturbance to the flow field.

The use of acoustics to obtain estimates of suspended sediment concentration in the ocean appears to have been first suggested by Dietz[1] in 1948. Little was done for many years, but progress has been rapid in the past decade.[2–7] Although these investigations have demonstrated the potential of acoustic remote sensing techniques for sediment transport studies, a remaining difficulty is the choice of the most appropriate acoustic model for the suspended particles. Such a model is needed to properly interpret the relationship between the measured acoustic signal and particle concentration and size.

The purpose of this article is to explore the usefulness of several theoretical models in which the scatterer, a sand grain, is approximated by a homogeneous solid sphere. The restriction to sand-sized material (63-μm to 2-mm diam) is important. The physical properties of naturally occurring particles, such as shape, density, and composition, vary significantly with size class. Therefore, it is expected that the scattering model most appropriate for sand could differ considerably from that for clay, for example (see Ref. 6).

Our objective is to determine whether the homogeneous sphere approximation is useful for sand grains and which spherical model, if any, is the most suitable. One of the motivations of the study was the existence in the literature of a considerable body of experimental data on both attenuation and scattering in aqueous suspensions of sand[4,7–9] that, with one exception,[4,10] had never been compared with the complete theory for scattering by a sphere. In this respect, the attenuation experiments by Flammer[8] are of particular importance since they represent the most comprehensive set of measurements to date.

The theoretical estimates are made for an inviscid, non-heat-conducting fluid and a homogeneous, spherical, non-heat-conducting particle. The particle is assumed to be either elastic, rigid and movable, or both rigid and immovable. By "elastic" we mean that shear and compression waves may propagate within the material and that the incident wave can induce displacements of the particle's center of mass. In a rigid particle, no sound propagation occurs. An immovable particle is infinitely dense. Comparisons are also made with a modified form of the so-called high-pass model introduced by Johnson.[11]

In addition to Flammer,[8] the data sources include Jansen,[9] Young *et al.*,[4] and Schaafsma and der Kinderen.[7] Flammer[8] made direct measurements of the additional attenuation caused by suspended sediment at 2.5, 5, 7.5, 10, and 15 MHz at a concentration of 2.65 kg/m^3. The samples were sieved into 17 size fractions in the 22- to 500-μm radius range. Both Jansen[9] and Schaafsma and der Kinderen[7] measured the scattered intensity as a function of sand concentration and size for a scattering angle of 120° in bistatic systems. The attenuation coefficient was obtained from the dependence of the scattered signal on concentration. Jansen's[9] measurements were made at 8 MHz in the concentration range 0.1–30 kg/m^3 and for four sieve fractions in the range of 50–280 μm. Schaafsma and der Kinderen[7] used 4.5-MHz systems and natural sand size distributions in the 50- to 100-μm range. The measurements were made at concentrations less than 5 kg/m^3. Young *et al.*[4] measured the backscatter intensity at 3 MHz for three size fractions in the 50- to 250-μm range. The concentrations were less than 0.1 kg/m^3.

In Sec. I, we begin with a brief summary of the theory, including an extension of Johnson's high-pass model for scattered intensity to include the dependence on scattering angle. In Sec. II, we develop a similar model for the attenuation coefficient. This is followed in Sec. III by comparisons between theory and experiment.

I. THEORY

A. The scattered pressure

Assume a plane wave incident on a homogeneous spherical particle surrounded by a uniform inviscid fluid. Ignoring attenuation for the moment, the scattered pressure at any field point far from the particle is given by

$$p_s = p_i\{[af_\infty(\theta,a)/2r]\}\exp[i(k_c r-\omega t)], \tag{1}$$

where p_i is the pressure amplitude of the incident wave, a is the particle radius, $f_\infty(\theta,a)$ is the farfield form factor, θ is the scattering angle, r is the radial distance from the particle, k_c is the acoustic wavenumber in the fluid, and ω is the angular frequency.

Consider now the wave scattered from an ensemble of particles of nonuniform size in the bistatic case. The bistatic geometry is considered here because two of the data sets to be used were acquired with bistatic systems. The equivalent results for monostatic systems are obtained simply as a special case. The geometry is shown in Fig. 1. The transmitting and receiving transducers (T and R in Fig. 1) are assumed to be circular and of equal diameter. The distance from the transmitter to an arbitrary particle is the incident path length and is denoted by r_i. The scattered path length is r_s, r_0 is the distance from either transducer to the center of the detected volume, and β_0 is the half-width of the mainlobe of the directivity pattern (i.e., $2\beta_0$ is the angular separation of the $-$3-dB points). We assume that the beamwidth is narrow. For the experiments discussed here, for example, β_0 is about 1°.

The pressure of the wave scattered from the particle is given by

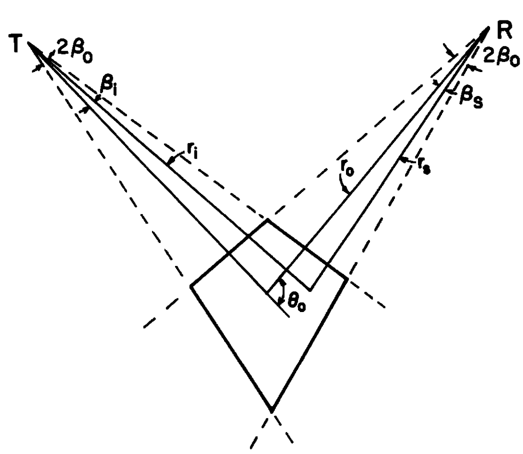

FIG. 1. The geometry for the bistatic case. T is the transmitter and R is the receiver. The remaining symbols are defined in the text.

$$p_s = (p_0 r_*/2r_i r_s)D_i D_s a f_\infty(\theta,a) \times\exp[-\alpha(r_i+r_s)]\exp\{i[k_c(r_i+r_s)-\omega t]\}, \tag{2}$$

where r_* is the distance along the acoustic axis of the transmitter to the point at which the sound pressure level is p_0; D_i and D_s are the directivities of the transmitter and receiver, respectively; and α is the attenuation coefficient, which is assumed to be uniform along the incident and scattered paths.

For a cloud of particles with an arbitrary distribution of sizes, the ensemble mean-square pressure in the absence of multiple scattering is given by

$$\hat{p}_s^2 = \int\int_\tau\int N\left(\int_0^\infty p_s p_s^* n(a)da\right)d\tau, \tag{3}$$

where $n(a)$ is the size spectral density, N is the number of particles per unit volume, the asterisk denotes the complex conjugate, and τ is the detected volume. Multiple scattering effects are ignored here because the data used were all acquired at concentrations less than 10 kg m^{-3}. As discussed in the Appendix, these concentrations are sufficiently dilute such that multiple scattering should not be important (see, also, Refs. 12 and 13). Substituting Eq. (2) gives

$$\hat{p}_s^2 = \frac{3Mp_0^2 r_*^2}{16\pi\rho_0'}\int\int_\tau\int\left[\frac{D_i^2 D_s^2}{r_i^2 r_s^2}\exp[-2\alpha(r_i+r_s)] \times\left(\int_0^\infty a^2|f_\infty(\theta,a)|^2 n(a)da\bigg/\int_0^\infty a^3 n(a)da\right)\right]d\tau, \tag{4}$$

where M is the mass concentration of suspended matter and is given by

$$M = N\rho_0'\frac{4}{3}\pi\int_0^\infty a^3 n(a)da, \tag{5}$$

with ρ_0' being the density of each particle.

The assumption of narrow beamwidth permits the following simplifications: $n(a)$ does not vary within the detected volume, $|f_\infty(\theta,a)|^2 = |f_\infty(\theta_0,a)|^2$ (see Fig. 1 for the definition of θ_0), and $r_s,r_i\sim r_0$. After making these approximations and separating the attenuation coefficient into two terms, one due to the ambient fluid (α_0) and one due to scattering (α_s), Eq. (4) can be written in the form[12]

$$\hat{p}_s^2 = S^2 H_0^2\exp(-4\alpha_s r_0), \tag{6}$$

where S is given by

$$S^2 = (p_0^2\tau r_*^2/4r_0^4)G_0^2\exp(-4\alpha_0 r_0). \tag{7}$$

Both G_0 and S are constants that depend on the geometry of the system.

In Eq. (6), H_0 depends upon the magnitude of the form factor, as well as upon the size distribution and the concentration of the suspended particles, and has the form

$$H_0^2 = 3M/4\pi\rho_0' \times\left(\int_0^\infty|f_\infty(\theta_0,a)|^2 a^2 n(a)da\bigg/\int_0^\infty a^3 n(a)da\right). \tag{8}$$

For simplicity, $f_\infty(\theta,a)$ will be written as $f_\infty(\theta)$ in the following discussion.

Equations (6) and (8) are central to the rest of the discussion; for monostatic systems, these equations remain unchanged. Only the numerical value of G_0 and the expression for the detected volume τ in Eq. (7) are different.

B. Form factor, total scattering cross section, and attenuation coefficient

Following Faran,[14] the form factor can be written in the form

$$f_\infty(\theta) = -\frac{2}{x}\sum_{n=0}^{\infty}(2n+1)\sin\eta_n \times\exp(-i\eta_n)P_n(\cos\theta), \quad (9)$$

where $x = k_c a$, η_n is the phase shift of the nth partial scattered wave, and P_n is the Legendre polynomial of order n.

The total scattering cross section is given by the usual result[15,16]

$$\Sigma_s = \frac{2\pi a}{k_c}\,\mathrm{Im}[f_\infty(0)], \quad (10)$$

which can be obtained directly from Eqs. (1) and (9). For uniformly sized particles, the attenuation coefficient due to scattering is given by $\alpha_s = N\Sigma_s/2$, or

$$a\alpha_s/\epsilon = \tfrac{3}{4}\{\mathrm{Im}[f_\infty(0)]/x\}, \quad (11)$$

using Eq. (5), where $\epsilon = M/\rho_0'$ is the volume concentration of suspended particles. For nonuniform particles, we have

$$\overline{\alpha}_s = \int_0^\infty \alpha_s n(a)da = 3\epsilon\int_0^\infty \mathrm{Im}[f_\infty(0)]an(a)da \Big/ 4k_c\int_0^\infty a^3 n(a)da. \quad (12)$$

The elastic properties of the scatterer enter the problem through the phase shifts η_n, expressions for which are given elsewhere.[14,16] The elastic properties of the scatterer depend on only three parameters involving scatterer properties: the ratio of the grain density to the fluid density, ρ_0'/ρ_0; $x' = k_c' a$; and $s' = k_s' a$. Here, k_c' and k_s' are, respectively, the wavenumbers of the compression and shear waves in the particle. For the rigid movable case, $x', s' \to 0$ since the phase speeds of compression and shear waves become infinite in a completely rigid material. For the rigid immovable case, in addition to the conditions above, $\rho_0'/\rho_0 \to \infty$.

C. High-pass model

Johnson[11] introduced the high-pass model for backscattered intensity. The essential idea is that a simple polynomial can be used to represent the overall x dependence of $|f_\infty|$ approximately by requiring that it fit this behavior exactly in the Rayleigh and geometric scattering regions, that is, where $|f_\infty|$ is, respectively, proportional to x^2 and equal to 1. We have extended this idea to include the angular dependence. The expression takes the form[12]

$$|f_\infty(\theta)| = K_f x^2/(1 + K_f x^2), \quad (13)$$

where $K_f = (\tfrac{2}{3})|\gamma_\kappa + \gamma_\rho\cos\theta|$ and γ_κ and γ_ρ are the usual compressibility and density contrasts in the Rayleigh range (e.g., Ref. 5). It can be seen that, for small x, Eq. (13) exhibits the required Rayleigh dependence on x and θ. For large x, $|f_\infty(\pi)|$ goes to unity as required. Equation (13) is also isotropic at large x. As will be seen, this may be a useful property.

We have also constructed a high-pass model for the attenuation coefficient which can be written as

$$a\alpha_s/\epsilon = K_\alpha x^4/[1 + (\tfrac{4}{3})K_\alpha x^4 + \xi x^2], \quad (14)$$

where $K_\alpha = (\gamma_\kappa^2 + \gamma_\rho^2/3)/6$ and ξ is an adjustable constant $\geqslant 1$. In this article, the value of ξ is chosen as 1. Equation (14) also displays the appropriate dependence on x and K_α in the Rayleigh and geometric regions. This is verified most readily perhaps by rewriting (14) in terms of the total scattering cross section Σ_s, which equals $8\pi a^2 x^4 K_\alpha/3$ and $2\pi a^2$ at small and large x, respectively.[15] The purpose of the ξx^2 term is to improve the fit to the data at intermediate values of x.

II. RESULTS

A. Attenuation coefficient

1. Flammer's[8] data

The attenuation coefficients measured by Flammer[8] for a mixture of Missouri River sand and blasting sand are shown in Fig. 2. The data are taken from Flammer's Fig 3.[8] Only those data points for mean diameters less than 500 μm are plotted since the data for larger sizes were considered to be less accurate.[8] The theoretical estimates assuming uniform particle size for the different models discussed in Sec. I are also plotted in Fig. 2 as solid lines. Figure 2(a)–(d) shows the comparisons between theory and experiment for the elastic, rigid movable, rigid immovable, and high-pass models, respectively. The residuals, the differences between the measured and theoretical estimates, are plotted for each case.

Consider first only those models that contain the most physics, that is, the elastic, rigid movable, and rigid immovable models. For convenience, we shall call these the "physical" models. The theoretical calculations were made with the following parameter values: for the elastic case, $\rho_0' = 2.65$ g cm^{-3} and compression and shear wave speeds of 5100 and 3200 m s^{-1}, respectively; for the rigid movable case, the same value of ρ_0', but with infinite wave speeds; and for the rigid immovable case, infinite density and infinite wave speeds. The number of terms retained in the partial wave expansion at each value of x was such that the ratio of the last term and the sum was less than 10^{-5}. The resolution of the calculations is 0.01 in x.

To begin, consider the elastic case [Fig. 2(a)]. The extrema in the theoretical curve near $x = 5.7$, 8.2, etc., in Fig. 2(a) are associated with the S_{21}, S_{31}, and higher-order Rayleigh wave resonances.[16] These features do not appear in Flammer's[8] data.

It can also be seen that, for $x \lesssim 2$, both the elastic and the rigid movable cases [Fig. 2(b)] fit the data reasonably well, and much better than the rigid immovable case [Fig. 2(c)]. For large values of x (>10), both rigid models give results that agree rather well with the data.

The attenuation coefficient α_s can also be normalized by $1/k_c\epsilon$ [Eq. (12)]. This normalizing factor has the advan-

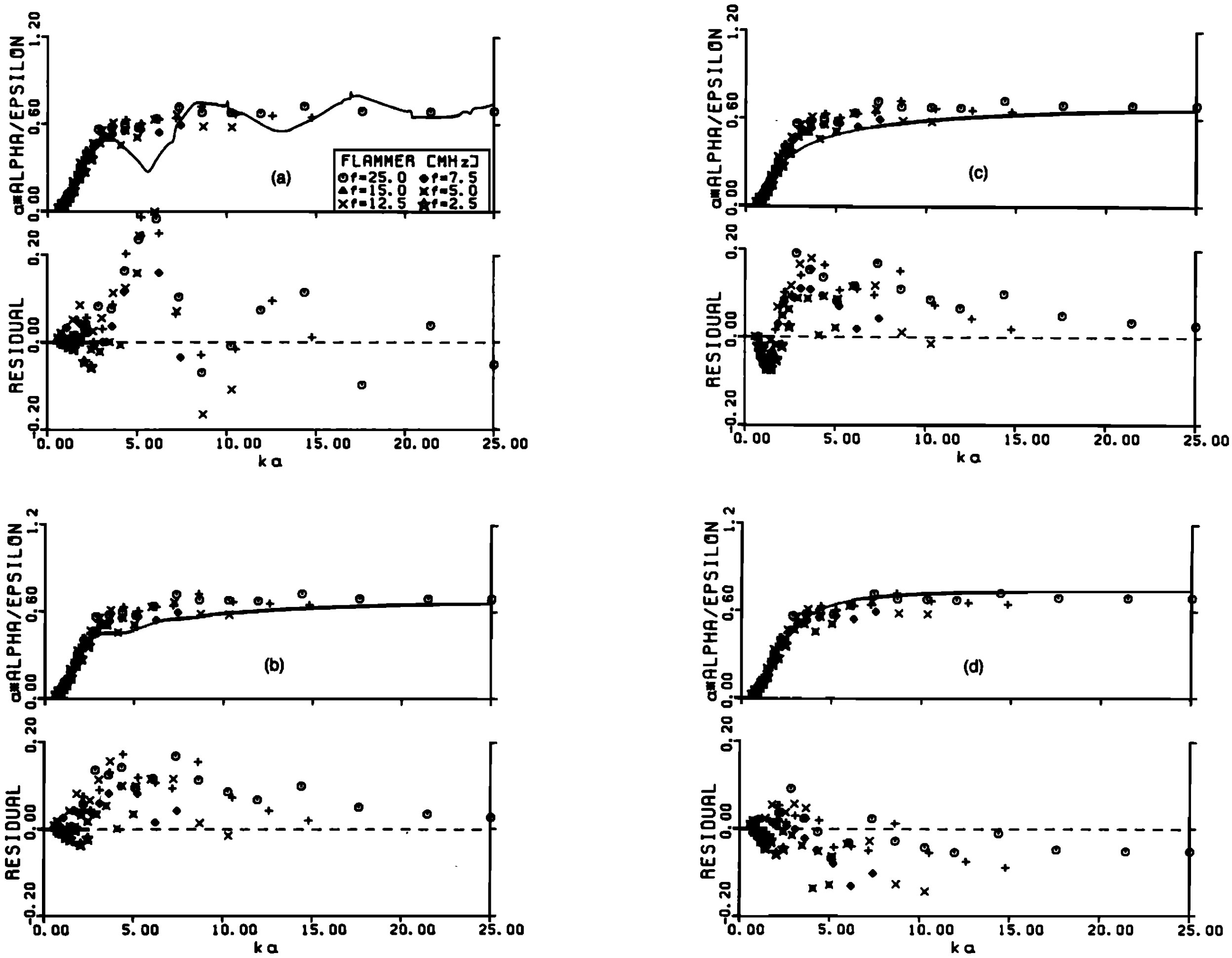

FIG. 2. Comparison of measured and computed values of $a\alpha_s/\epsilon$ using Flammer's[8] data. The solid lines in (a) and (b) are the theoretical results for (a) the elastic case using $\rho_0' = 2.65$ g cm^{-3} and compression and shear wave speeds of 5100 and 3200 m s^{-1}, respectively; and (b) the rigid movable case with $\rho_0' = 2.65$ g cm^{-3} and infinite shear and compression wave speeds. The solid lines in (c) and (d) are the theoretical results for (c) the rigid immovable case (infinite ρ_0' and sound speeds in the particle) and (d) the high-pass model.

tage that the measured values of α are not multiplied by a, which is not well defined for nonuniform sizes [Eq. (12)] and therefore introduces another source of error into the comparisons. A plot of $\alpha_s/k_c\epsilon$ vs x for the rigid movable case is shown in Fig. 3. In Fig. 3, the generally good agreement between theory and experiment is again apparent. It is clear, however, that the observed attenuation coefficients are larger than those predicted in the region $2 < x < 7$. This same effect is seen in Fig. 2; we must now conclude that it does not result from the normalization procedure.

For quantitative comparison, two measures are used here: the correlation coefficient R_{yz} and the percentage difference d, which is given by

$$d = \frac{1}{m} \sum_{i=1}^{m} \frac{|y_i - z_i|}{z_i}, \tag{15}$$

where y_i and z_i are, respectively, the theoretical and experimental estimates for the same x and m is the number of measurements. The percentage differences and correlation coefficients for the various cases and uniform size are given

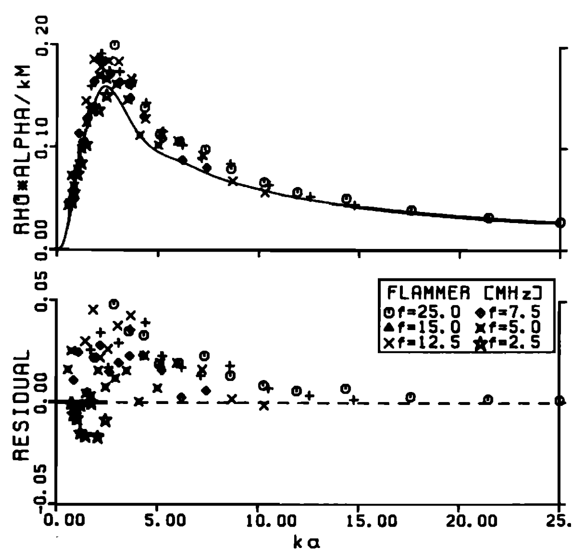

FIG. 3. Comparison of measured and computed values of $\alpha_s/k_c\epsilon$ using Flammer's[8] data. The solid line is the theoretical result in the rigid movable case.

TABLE I. The percentage differences and correlation coefficients (in parentheses) between computed and measured $a\alpha_s/\epsilon$ using Flammer's[8] data.

Case	Uniform	Log normal
Elastic	15.3 (0.903)	14.0 (0.943)
Rigid movable	13.1 (0.979)	13.2 (0.979)
Rigid immovable	20.9 (0.964)	19.7 (0.964)
High pass	10.7 (0.980)	11.0 (0.978)

in Table I. From Table I, we see that the physical model providing the worst agreement is either the elastic case (correlation coefficient 0.90), or the rigid immovable case (percentage difference 21), depending on which of the two quantitative measures is used. Both the percentage difference and the correlation coefficient attain their best values for the rigid movable case.

Some reduction in the percentage differences is to be expected if the size distributions are included in the computations since this would effectively cause additional smoothing of the theoretical results. The size parameters given by Flammer[8] for each sand fraction were those for the log-normal distribution, which has the form

$$n(\ln a) = (1/\sqrt{2\pi}\ln\sigma_g)\times\exp[-(\ln a - \ln a_g)^2/2\ln^2\sigma_g], \quad (16)$$

where a_g and σ_g are, respectively, the geometric mean radius and the geometric standard deviation. The effect on the theoretical results for the rigid movable case is illustrated in Fig. 4. The calculations were made with $\sigma_g = 1.2$, the value given by Flammer.[8] Only a modest amount of smoothing occurs; consequently, it is not surprising that only minor changes in the percentage differences and correlation coefficients result (Table I). Therefore, it appears that the absence of resonance features in the data [Fig. 2(a)] is not ascribable to the smoothing effects of the size distribution.

Returning to Fig. 2, it can be seen that the high-pass model [Eq. (14)] provides a very reasonable fit to the data [Fig. 2(d)]. In fact, for Flammer's[8] data set this fit is as good or better than the best physical model, the rigid movable case (Table I). This model may therefore prove to be a useful approximation for sound attenuation in aqueous suspensions of irregularly shaped particles such as sand grains.

Finally, as a basis for direct visual comparison with the results presented below, in Fig. 5 the computed attenuation coefficients for each of the models assuming uniform size are plotted against the measurements in the form of scatter diagrams.

2. Other experiments

Attenuation measurements in sand suspensions have been made more recently by Jansen[9] and Schaafsma and der Kinderen.[7] These results and the values of x at which they were made are listed inTable II (see, also, the Appendix), together with the computed values for the different models assuming uniform size. There are not a large number of data and most are for values of $x < 2$. Nevertheless, these results

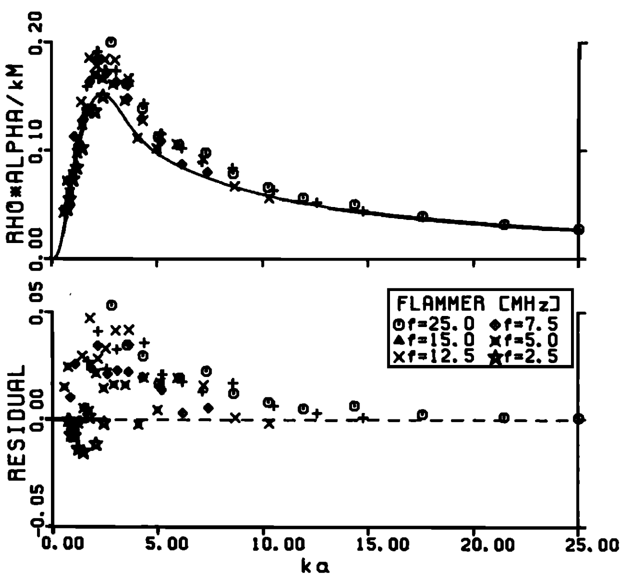

FIG. 4. Comparison of measured and computed values of $\alpha_s/k_c\epsilon$ using Flammer's[8] data. The solid line is the theoretical result for the rigid movable case for log-normal size distribution with $\sigma_g = 1.2$.

support the conclusions drawn above. This may be seen by comparing Figs. 6 and 5, or by examining the quantitative measures of comparison in Table III. Again, depending upon one's choice of the measure of agreement, either the elastic or the rigid immovable model provides the worst fit to the data and the rigid movable and high-pass models provide the best.

This conclusion holds whether the effects of the finite width size distribution are included or not. For these data, it was more convenient to use Gaussian and Rayleigh distributions to fit the size parameters given. The Gaussian distribution simply took its usual form:

$$n(a) = (1/\sqrt{2\pi}\sigma)\exp[-(a-\bar{a})^2/2\sigma^2], \quad (17)$$

where $\bar{a}$ and σ are, respectively, the mean value and the standard deviation. The Rayleigh distribution used here is a modified version of the usual form and is given by

$$n(a) = [\pi(a-l)/2\bar{a}_0^2]\exp[\pi(a-l)^2/4\bar{a}_0^2], \quad (18)$$

where $n(a) = 0$ for $a \leqslant l$. In Eq. (18), $\bar{a}_0$ determines the shape of the distribution. The mean size $\bar{a}$ is given by $(\bar{a}_0 + l)$.

The percentage differences and correlation coefficients for all cases are presented in Table III. The values of σ and $\bar{a}_0$ used in the computations are given in Table IV. Again, as was the case with Flammer's data (Table I), the effects of including the size distributions in the calculations are small.

B. Scattered intensity

No absolute measurements of scattered intensity are available. Instead, researchers have presented results in terms of the mean-square voltage ($\overline{V}_s^2$) output from the receiver. In order to compare measured and theoretical scattered intensities, the $\overline{V}_s^2$ values were normalized by the aver-

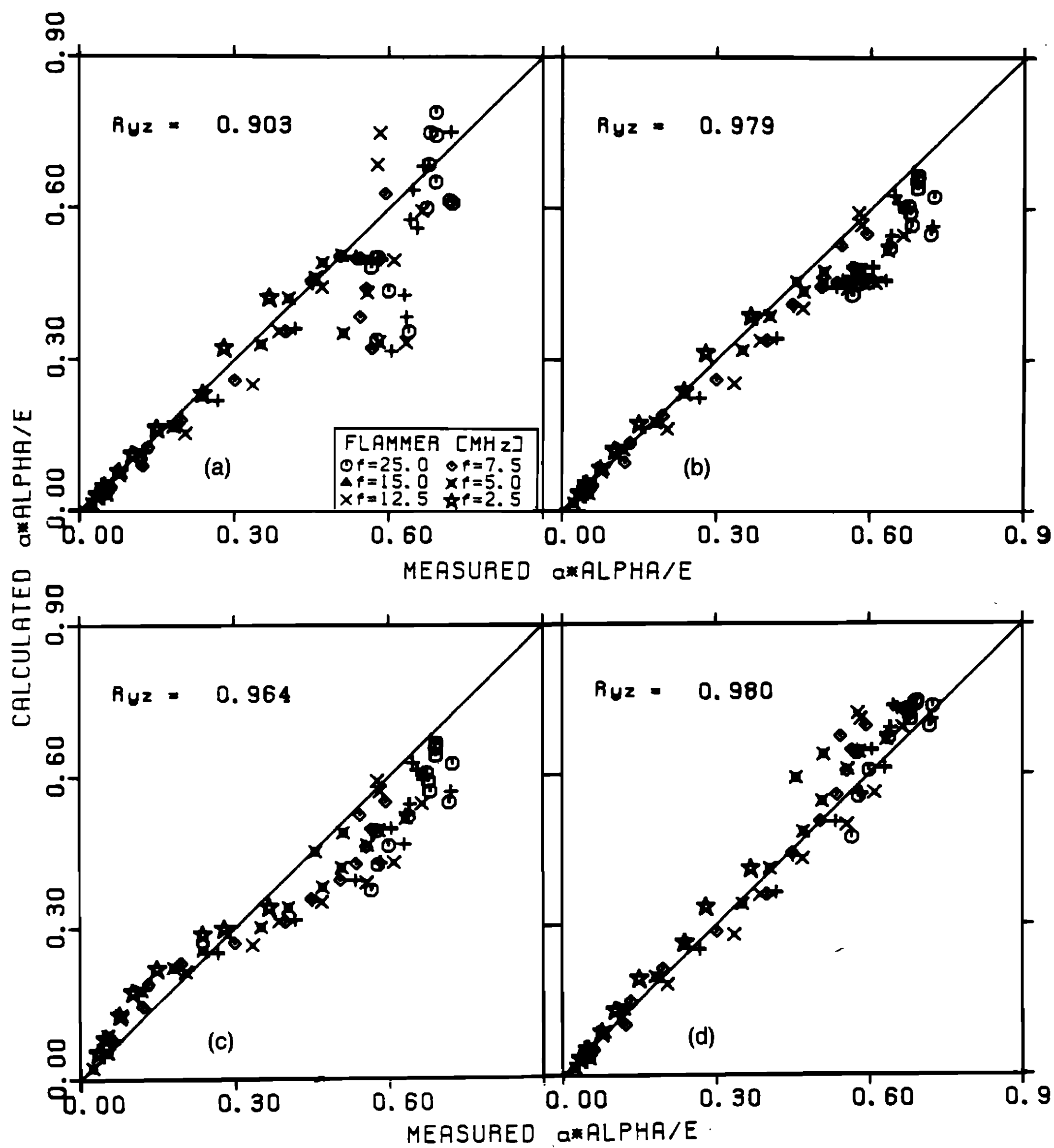

FIG. 5. Comparison between calculated and measured values of $\bar{a}\alpha_s/\epsilon$ for Flammer's[8] data, where the calculations are for uniform particle size in (a) the elastic case, (b) the rigid movable case, (c) the rigid immovable case, and (d) the high-pass model.

TABLE II. Calculated and measured values of $\bar{a}\alpha_s/\epsilon$ assuming uniform particle size. "Movable" and "immovable" refer to the rigid movable and rigid immovable cases, respectively.

	Sand		$\bar{a}\alpha_s/\epsilon$	$\bar{a}\alpha_s/\epsilon$			
Source	$\bar{a}$ (μm)	$k_c\bar{a}$	Measured	Elastic	Movable	Immovable	High pass
Jansen[9,24]	54	1.84	0.256,0.178	0.262	0.263	0.272	0.289
	115	3.96	0.566,0.531	0.473	0.455	0.444	0.583
	193	6.60	0.706,0.522	0.448	0.539	0.536	0.683
	275	9.43	⋯ ,0.655	0.731	0.582	0.582	0.716
Schaafsma and	50	0.96	0.067	0.066	0.071	0.110	0.072
der Kinderen[7]	80	1.54	0.168	0.182	0.191	0.233	0.214
(1D)	100	1.93	0.235	0.288	0.286	0.284	0.300
Schaafsma and	50	0.96	0.075	0.066	0.071	0.110	0.072
der Kinderen[7]	75	1.45	0.176	0.162	0.171	0.219	0.192
(2D)	100	1.93	0.242	0.288	0.286	0.284	0.310

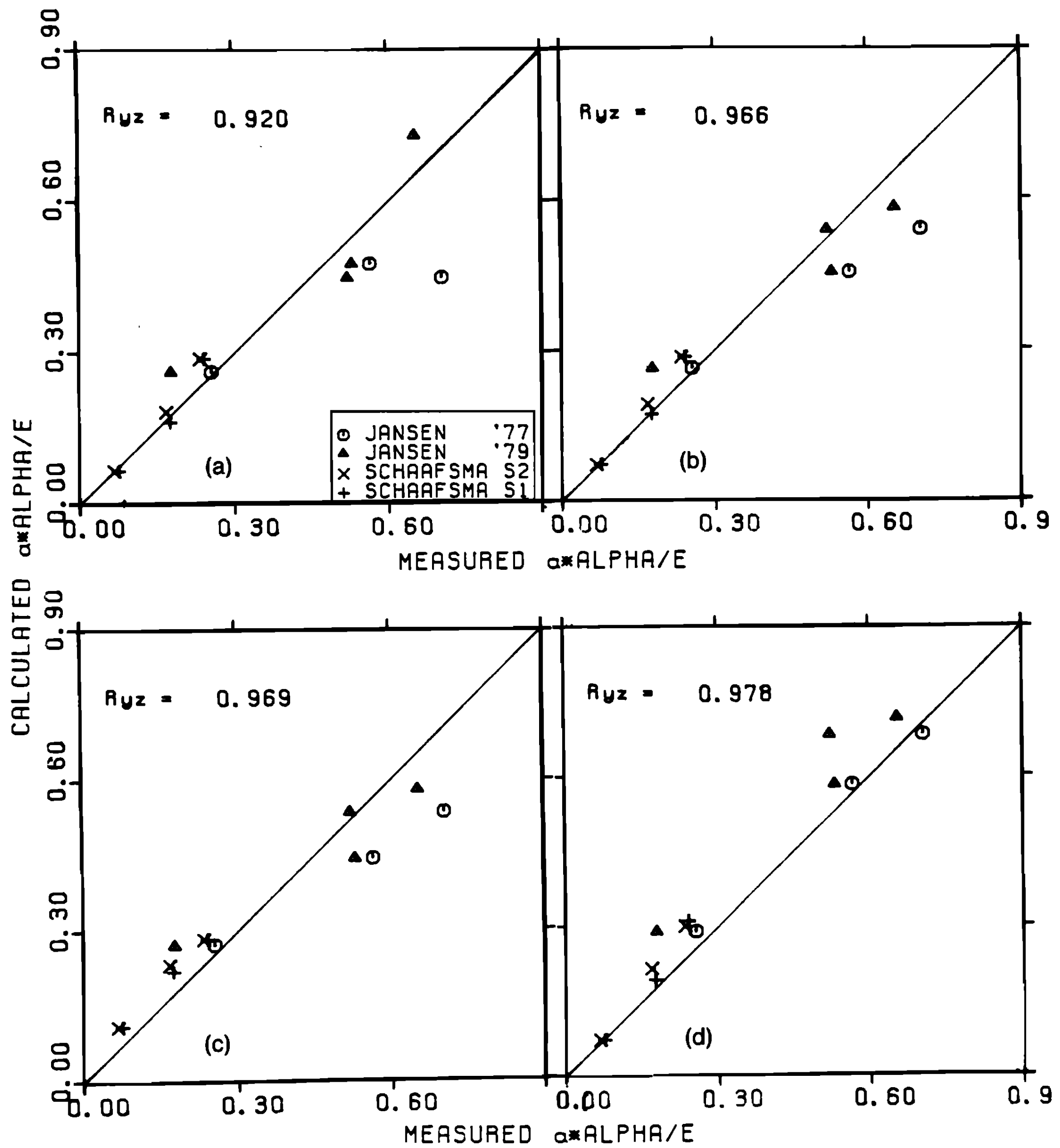

FIG. 6. Comparison between calculated and measured values of $\bar{a}\alpha_s/\epsilon$ for Jansen's[9,24] and Schaafsma and der Kinderen's[7] data, where the calculations are for uniform particle size in (a) the elastic case, (b) the rigid movable case, (c) the rigid immovable case, and (d) the high-pass model.

age over all size fractions in each data set. Similarly, using Eq. (8), the theoretical estimates of H_0^2 were computed for each size fraction and normalized by the average of the values for all size fractions for each data set.

The comparisons between the normalized values of H_0^2 and $\overline{V}_s^2$ for uniform particle size are shown in Fig. 7. Note that the experimental results obtained by Young *et al.*[4] (see,

TABLE III. Percentage differences and correlation coefficients (in parentheses) as in Table I using Jansen's[9,24] and Schaafsma and der Kinderen's[7] data.

Case	Uniform	Gaussian	Rayleigh
Elastic	16.2 (0.920)	14.9 (0.925)	15.0 (0.924)
Rigid movable	14.7 (0.966)	12.7 (0.972)	13.3 (0.971)
Rigid immovable	26.6 (0.969)	21.3 (0.970)	24.1 (0.956)
High pass	18.1 (0.978)	15.3 (0.979)	15.6 (0.979)

TABLE IV. The size distribution parameters.

Source	Size range (μm)	Gaussian σ (μm)	Gaussian $\bar{a}$ (μm)	Rayleigh $\bar{a}_0$ (μm)	Rayleigh $\bar{a}$ (μm)
Jansen[9,24]	45–63	9	54	18	55
	105–125	10	115	20	116
	175–210	18	192	35	195
	250–300	25	275	53	277
Schaafsma and	38–60	11	49	23	51
der Kinderen[7]	55–108	27	79	51	82
(1D)	65–125	30	99	65	103
Schaafsma and	38–60	11	49	23	51
der Kinderen[7]	55–108	27	79	51	82
(1D)	65–125	30	99	65	103
Schaafsma and	34–70	19	49	34	51
der Kinderen[7]	53–120	34	74	55	78
(2D)	75–160	43	99	66	103
Clarke *et al.*[10]	37–55	9	47	19	47
Minor axis	70–90	11	81	21	83
	153–227	38	191	75	270

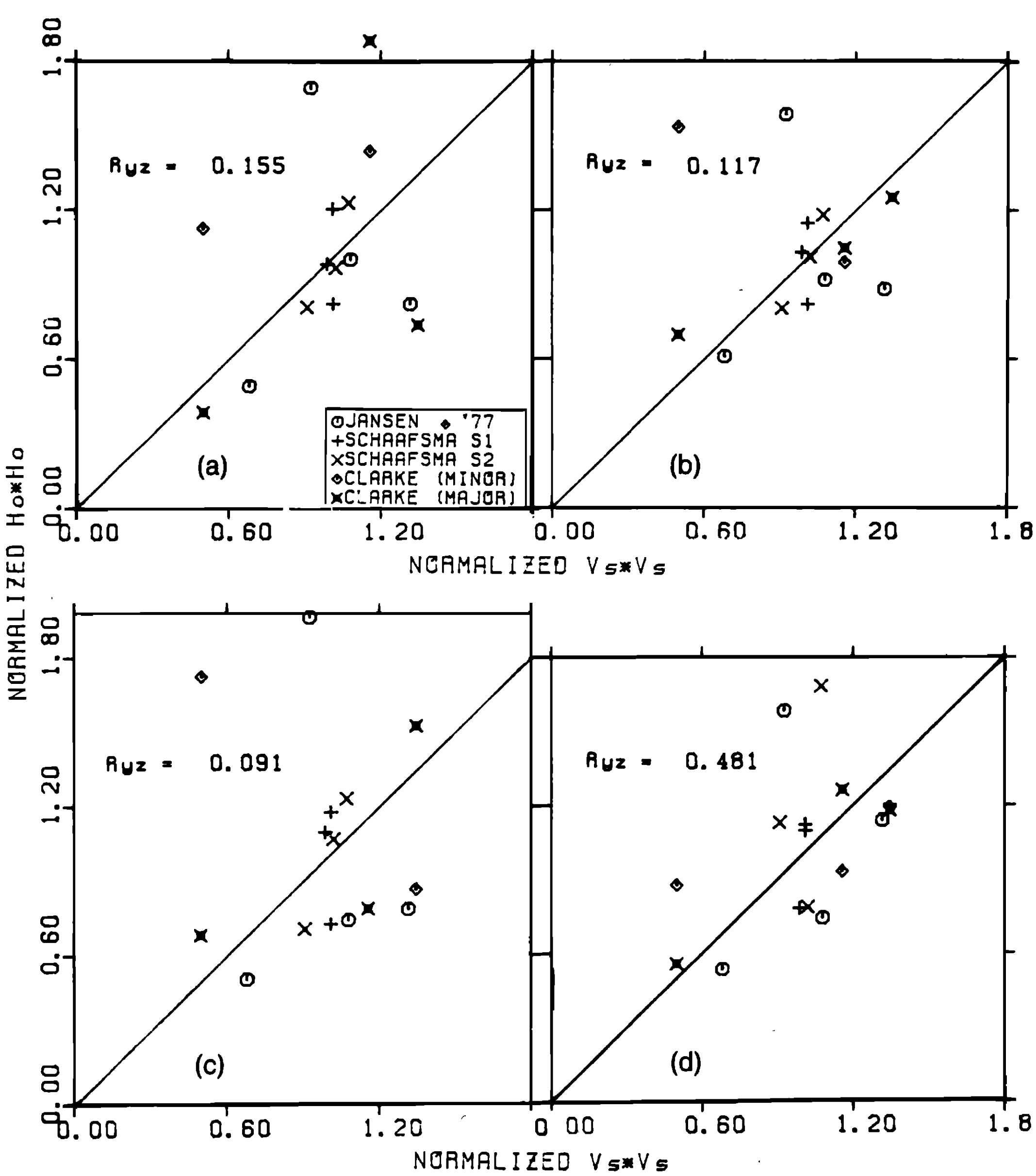

FIG. 7. Normalized values of H_0^2 and $\overline{V_s^2}$ for uniform size in (a) the elastic case, (b) the rigid movable case, (c) the rigid immovable case, and (d) the high-pass model.

also, Ref. 10) using a monostatic system have been included. It is immediately apparent, comparing Fig. 7 with Figs. 5 and 6, that there is much more scatter in the comparisons for the available data on scattered intensity than for the data on attenuation. The percentage differences between the normalized estimates and theoretical values for all cases and three size distributions are presented in Table V. The percentage differences are large (25%–50%). These differences are too large to permit useful discrimination among the physical models, although the rigid movable model still provides the best fit.

TABLE V. The percentage differences and correlation coefficients (in parentheses) between normalized theoretical and measured scattered intensities.

Case	Uniform	Gaussian	Rayleigh
Elastic	35.9 (0.115)	27.6 (0.415)	26.6 (0.462)
Rigid movable	33.2 (0.117)	25.3 (0.319)	25.4 (0.392)
Rigid immovable	46.0 (0.091)	49.2 (0.117)	51.1 (0.101)
High pass	26.3 (0.481)	22.5 (0.473)	24.4 (0.459)

Some reduction in percentage difference is achieved if we follow the suggestion of Clarke *et al.*[10] and use the total scattering cross section to compute the scattered intensity at any given angle. The idea is that the random orientations of the irregularly shaped sand grains will cause the scattering to be more isotropic on average.[17] In this case, $|f_\infty(\theta)|^2$ in Eq. (8) should be replaced by $\langle |f_\infty|^2 \rangle$, where the angular brackets denote the average over all scattering angles from 0–π. Furthermore, the total scattering cross section in the isotropic limit becomes

$$\Sigma_s = \pi a^2 \langle |f_\infty|^2 \rangle, \tag{19}$$

TABLE VI. The percentage differences and correlation coefficients (in parentheses) between normalized values of $\langle H_0^2\rangle$ and normalized values of $\overline{V_s^2}$ percentage to computed scattered intensity.

Case	Uniform	Gaussian	Rayleigh
Elastic	29.9 (0.448)	27.0 (0.531)	28.0 (0.515)
Rigid movable	26.4 (0.554)	23.4 (0.605)	24.7 (0.584)
Rigid immovable	19.2 (0.659)	17.6 (0.668)	18.7 (0.662)
High pass	25.5 (0.594)	23.7 (0.620)	24.2 (0.613)

so that the attenuation coefficient $\overline{\alpha}_s$ in Eq. (12) can be written as

$$\overline{\alpha}_s = \frac{3\epsilon}{8}\left(\int_0^\infty a^2\langle|f_\infty|^2\rangle n(a)da\right)\Big/\left(\int_0^\infty a^3 n(a)da\right), \tag{20}$$

using Eqs. (10) and (19). Finally, comparing Eqs. (8) and (20), we obtain

$$\langle H_0^2\rangle = 2\overline{\alpha}_s/\pi, \tag{21}$$

where $\langle H_0^2\rangle$ denotes the value of H_0^2 after averaging over all possible orientations.

The normalized values of $\langle H_0^2\rangle$ were calculated using Eq. (21) and compared to the $\overline{V_s^2}$ data. The percentage differences and correlation coefficients for all cases are presented in Table VI. It can be seen that there is considerable improvement in the percentage differences and the correlation coefficients, specifically in the rigid immovable case, which now provides the best fit. These results suggest that this approach may be useful. The degree of scatter, however, remains large; in light of the attenuation results, the fact that the rigid immovable case emerges with the best fit seems suspect.

III. SUMMARY AND CONCLUSIONS

We have compared theoretical estimates of scattered intensity and the attenuation coefficient with data published previously for dilute aqueous suspensions of sand. The theoretical calculations are made by approximating the sand grain as a homogeneous spherical particle. Three model spheres are used: elastic, rigid movable, and rigid immovable.

This appears to be the first comparison of theoretical and experimental attenuation coefficients in suspensions of mineral grains at wavelengths comparable to or less than the scatterer circumference. As far as the existing data are concerned, these attenuation comparisons are crucial. The rigid movable case provides the best fit to the data. This, together with the fact that the rigid immovable case fits the data less well, indicates that the inertia of the particles is important, particularly for values of x near unity.

The fact that the elastic case does not fit the data as well as either rigid model indicates that resonance excitation does not occur, supporting a similar conclusion made by Clarke *et al.*[10] on the basis of comparisons between backscatter data and a fluid sphere model. This is probably because natural sand grains are irregularly shaped and inhomogeneous in composition. It is well known that resonance excitation by scattering can be described in terms of surface waves and that for a spherical scatterer the circuit times of the surface waves at resonance must be an integral dividend of the incident wave period.[18] It appears that in natural sand grains, the irregularities in shape are such that the surface waves have no well-defined circuit time; therefore, resonance does not occur.

The rigid movable model underpredicts the attenuation for intermediate values of x, however. Again, this probably arises from irregularities in grain shape. Additional scattering from surface roughness features is to be expected for values of $x > 2$. Similar effects have been observed in optical scattering experiments with irregular particles.[19] At large values of x, Flammer's data[8] asymptotically tend toward the geometric cross section of a perfect sphere. This may reflect either a lower limit to the surface roughness scale or problems with the measurements at large sizes.[8]

The comparisons using scattered intensities, however, exhibit a very high degree of scatter. Improved agreement is obtained by assuming that on average the scattering is isotropic. In addition to the possible inadequacies of the models, however, there are a number of other potential contributing factors. One factor is the normalization procedure, which would not contribute if absolute measurements had been made. A second factor is that it is difficult to make unambiguous estimates of the relative amplitudes of the scattered signals at different radii from some of the experiments. Third, it is possible that in Jansen's[9] experiments the particles adopted a preferred orientation because they were allowed to free fall through the detected volume. Regardless, a more comprehensive set of measurements is needed.

Approximate expressions for the form factor and attenuation coefficient have been constructed based on the so-called high-pass model introduced by Johnson.[11] Our modified high-pass model provides a fit to the attenuation data that is as good as or better than the rigid movable case. This model is therefore potentially valuable, providing a simple analytic expression for evaluation of the size and concentration dependence of the scattered signal.

Finally, comparisons have been made assuming that multiple scattering effects are small. The assumption is justified by examining the available data for nonlinearity in the attenuation as a function of concentration. Such nonlinearity appears only at concentrations exceeding 10 kg m^{-3} and the magnitude of the effect is shown to be roughly consistent with expectation.

ACKNOWLEDGMENTS

The authors wish to thank Dr. A. S. Schaafsma (Delft Hydraulics Laboratory) for useful comments on this manuscript, discussion of the experimental results, and for making data available to us. Funding was provided by the Natural Sciences and Engineering Research Council of Canada under Grant No. A8446 and the Canada Department of Energy, Mines and Resources under Research Agreement 152.

APPENDIX: MULTIPLE SCATTERING LIMIT

In this Appendix, we estimate the concentration at which multiple scattering becomes important. For simplicity, we initially assume isotropic scattering and particles of

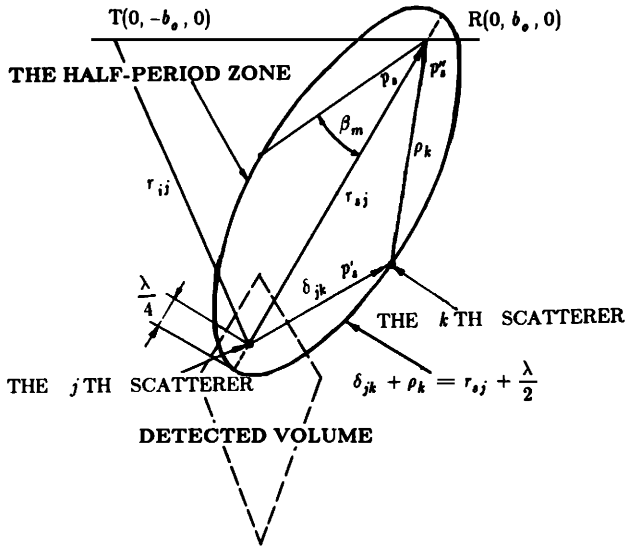

FIG. A1. The half-period zone for the first-order multiple scattered waves.

uniform size. Furthermore, because we are interested in approximate estimates only, the Waterman and Truell[20] formulation is used.

We choose two scatterers, the jth and the k th, and suppose the scattered pressure from the jth particle is rescattered by the k th scatterer. Referring to Fig. A1, the distance from the jth particle to the transmitter is r_{ij}, and to the receiver it is r_{sj}. The distance from the k th to the jth particle is δ_{jk}, and to the receiver it is ρ_k.

Following Waterman and Truell,[20] the Fresnel half-period zones are ellipsoids and the interior of the nth half-period zone is defined by $r_{sj}+(n-1)(\lambda/2)\leqslant\delta_{jk}+\rho_k\leqslant r_{sj}+n(\lambda/2)$, where n is an integer and λ is the acoustic wavelength. All waves rescattered by particles located within a given Fresnel zone have amplitudes of the same sign when they arrive at the receiver. On average, the contributions from adjacent zones will be opposite in sign; because of the attenuation and radial spreading of the scattered wave from the jth particle, we can say the total contribution from several zones could not be larger than the contribution from the first zone. As a result we need only consider multiple scattering from the first zone, the boundary of which is defined by $\delta_{jk}+\rho_k=r_{sj}+\lambda/2$ (see Fig. A1). The scattered and rescattered pressures are given by

$$p_{sj}=p_i(af_\infty/2r_{sj})\exp(ik_c r_{sj}), \quad \text{(A1)}$$

$$p_{sj}''=p_i(a^2f_\infty^2/4\rho_k\delta_{jk})\exp[ik_c(\delta_{jk}+\rho_k)], \quad \text{(A2)}$$

where p_{sj} is the pressure at the receiver of the wave scattered from the jth particle and p_{sj}'' is the received pressure of this same wave after being rescattered by the k th particle.

Let P_{1j} be the total (first-order) multiple scattered pressure from the first Fresnel half-period zone, so that we have

$$P_{1j}=N\int\int_{\text{zone }1}\int p_{sj}''\,d\tau. \quad \text{(A3)}$$

Substituting Eq. (A2) into (A3), we have

$$P_{1j}=\tfrac{1}{4}p_i a^2 f^2 N \times\int\int_{\text{zone }1}\int\left(\frac{1}{\delta\rho}\exp[ik_c(\delta+\rho)]\right)d\tau, \quad \text{(A4)}$$

where the subscripts on δ and ρ have been dropped for convenience.

Following Waterman and Truell,[20] we choose the bipolar coordinates ρ, δ, and Φ (the azimuthal angle about the acoustic axis) for the integration. In the first zone we have

$$r_{sj}\leqslant\delta+\rho\leqslant r_{sj}+\lambda/2 \quad \text{(A5)}$$

and

$$\begin{cases}0\leqslant\rho\leqslant r_{sj}+\lambda/4,\\ 0\leqslant\Phi\leqslant 2\pi.\end{cases} \quad \text{(A6)}$$

The volume element $d\tau$ is given by $d\tau=\delta\rho\,d\rho\,d\delta\,d\Phi/r_{sj}$ (see Ref. 21) so that after integrating Eq. (A4) we obtain

$$P_{1j}=[\pi i a f_\infty N(r_{sj}+\lambda/4)/k_c] \times p_i(af_\infty/r_{sj})\exp(ik_c r_{sj}). \quad \text{(A7)}$$

Equation (A7) can be written as

$$P_{1j}/p_{sj}=2\pi i a f_\infty N r_{sj}/k_c \quad \text{(A8)}$$

since $\lambda/4\ll r_{sj}$. For the narrow beam case we have $r_{sj}\approx r_0$ and Eq. (A8) becomes

$$P_{1j}/p_{sj}=2\pi i a f_\infty N r_0/k_c, \quad \text{(A9)}$$

which is similar to the result obtained by Waterman and Truell[20] [their Eq. (A6)].

If $|P_1/p_s|\ll 1$, then multiple scattering can be ignored. This condition holds if

$$N\ll k_c/2\pi a|f_\infty|r_0. \quad \text{(A10)}$$

By using Eq. (5) for uniformly sized scatterers, condition (A10) becomes

$$M/\rho_0'\ll 2x^2/3k_c|f_\infty|r_0. \quad \text{(A11)}$$

Let us consider cases in which $x\ll 1$, $a\sim 50\ \mu$m, $|f_\infty|\sim x^2$ [for quartzlike particles, see Eq. (13)], and $r_0\approx 0.1$ m. We obtain

$$M/\rho_0'\ll 5\times 10^{-3}. \quad \text{(A12)}$$

For quartz particles, $\rho_0'\sim 3\times 10^3$ kg/m^3, giving $M\ll 15$ kg/m^3.

Condition (A11) can be too restrictive, however, because the transducer directivity has not been considered. From Fig. A1 it can be shown that β_m, the angle subtended by half the minor axis of the first zone, is given by

$$\cos\beta_m=(r_{sj}/2)/(r_{sj}/2+\lambda/4)\approx 1-\lambda/2r_{sj} \quad \text{(A13)}$$

and, since $r_{sj}\approx r_0$,

$$\beta_m\approx\sqrt{\lambda/r_0}=\sqrt{c/r_0 f}. \quad \text{(A14)}$$

Considering a typical case where $r_0=0.15$ m, the frequency $f=8$ MHz, $\beta_0=1°$, and the speed of the sound $c=1500$ m s^{-1}, we obtain $\beta_m\approx 2°$. Therefore,

$$\beta_m\approx 2\beta_0. \quad \text{(A15)}$$

From Eq. (A15) we note that the mainlobe of the receiver beam pattern is inside the first Fresnel zone. Since the receiver is sensitive primarily to the waves scattered from the particles that are located in the mainlobe, the total multiple scattered pressure calculated by Eq. (A3) is therefore larger than that actually sensed by the receiver. In other words, the actual value of maximum concentration for ignoring the multiple scattering could be larger than that estimated from Eq. (A11).

The results obtained above require that x should be small, so that the form factor is independent of scattering angle. For other values of x, the isotropic assumption does not hold and, for x large enough, $|f_\infty|$ becomes very large in the forward direction (see Ref. 15). This permits us to consider multiple scattering only in this direction. The rescattered pressure in Eq. (A2) now takes the form

$$p''_{sj} = p_i [4a^2 f_\infty(\theta) f_\infty(0)/\rho_k \delta_k] \exp[ik_c(\delta_{jk} + \rho_k)] \tag{A16}$$

since $\delta_{jk} + \rho_k = r_{sj}$. The total (first-order) multiple scattered pressure in the forward direction P_{1j} is given by

$$P_{1j} = [p_i a^2 f_\infty(\theta) f_\infty(0)/4] \exp(ik_c r_{sj}) \times \sum_{k=1} \frac{1}{\delta_{jk}(r_{sj} - \delta_{jk})}. \tag{A17}$$

Let Δ be the average interval between any two neighboring particles. Clearly, Δ is equal to $1/N^{1/3}$. Then, Eq. (A17) becomes

$$P_{1j} = [p_i a^2 f_\infty(\theta) f_\infty(0)/4] \exp(ik_c r_{sj}) \times \int_\Delta^{r_{sj} - \Delta} \frac{1}{\delta(r_{sj} - \delta)} \frac{d\delta}{\Delta}. \tag{A18}$$

After integrating Eq. (A18) and assuming $r_{sj} \gg \Delta$, we obtain

$$P_{1j} = \frac{f_\infty(0)a}{2\Delta} \left(\frac{p_i a f_\infty(\theta) \exp(ik_c r_{sj})}{2 r_{sj}} \right) \left(2 \log \frac{r_{sj}}{\Delta} \right) \tag{A19}$$

or

$$P_{1j}/p_{sj} = N^{1/3} f_\infty(0) a \log(N^{1/3} r_{sj}). \tag{A20}$$

Consider a typical case with uniform-sized scatterers of radius $a = 300\ \mu$m and $x = 10$. It can be shown[12] that $|f_\infty(0)|$ increases linearly with x for $x > 1$, so that $|f_\infty(0)| \approx 10$. Therefore, with $r_0 = 0.15$ m, Eq. (A20) gives $M \ll 2.0$ kg m^{-3} as the condition for negligible multiple scattering. It can be seen that, as the amplitude of the forward scattered wave increases, the maximum concentration for ignoring multiple scattering decreases.

We now consider the observations. The mean-square output voltage from the receiver, divided by the concentration M, is plotted against M using Jansen's[9] data in Fig. A2 and Schaafsma and der Kinderen's[7] results in Fig. A3. It can be seen that, for the most part, the data are consistent with the attenuation being a linear function of concentration, as expected in the absence of multiple scattering [Eqs. (6) and (11)]. In Jansen's[9] data, however, there is an indication of nonlinear behavior at the highest concentrations [Fig. A2(b)]. The nonlinearity is such that the increased attenuation per unit increase in concentration decreases, a well-known effect of multiple scattering.[22,23]

The measurements exhibiting nonlinear behavior are for two sand sizes: 54- and 115-μm mean radius, corresponding to values of x of 1.84 and 3.96, respectively. Using Eq.

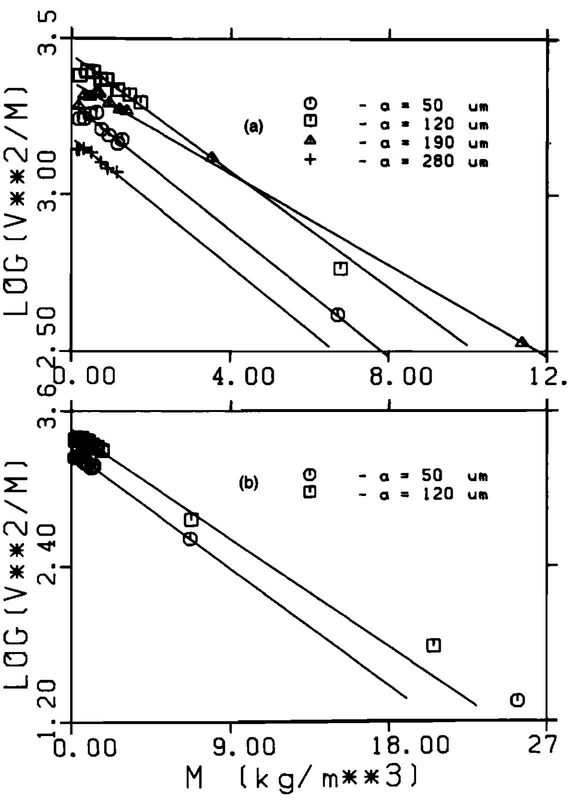

FIG. A2. $\text{Log}_{10}(\overline{V_s^2}/M)$ vs M for data given by Jansen.[24] (a) Low concentrations and (b) the entire range of concentration in the experiments for $\bar{a} = 50$ and $120\ \mu$m.

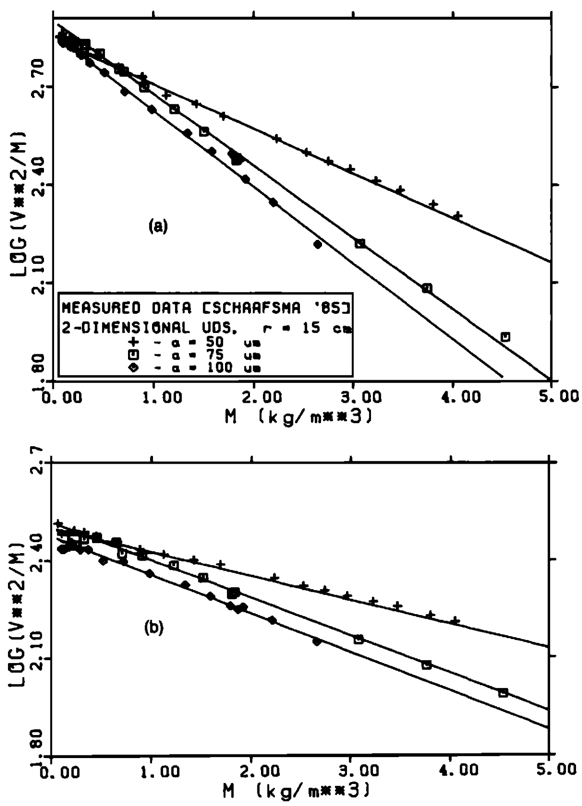

FIG. A3. $\text{Log}_{10}(\overline{V_s^2}/M)$ vs M for data given by Schaafsma and der Kinderen.[7] (a) From S_2^2 and (b) from S_1^2.

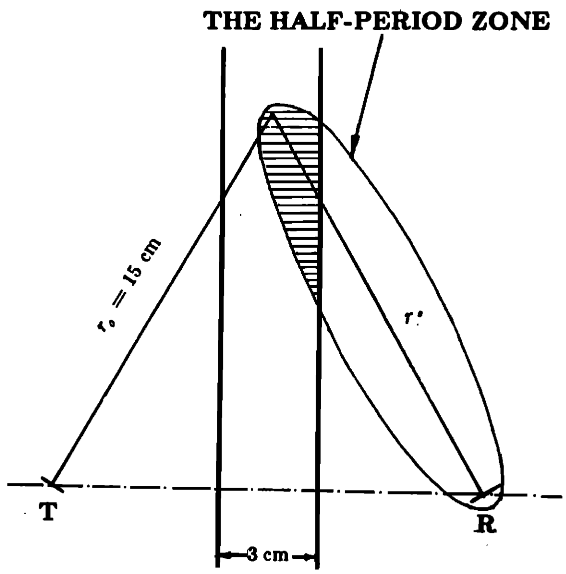

FIG. A4. The geometry in Jansen's[9,24] experiments. The 3-cm-wide rectangular perspex tube through which the sand grains were allowed to fall is shown in the center of the figure.

(9), the form factor $|f_\infty|$ has been calculated for three scattering angles: 0°, 120°, and 180°. For $x = 1.84$, the values are 0.77, 0.71, and 0.68, respectively. These are nearly the same and the isotropic scattering model is assumed in this case. For $x = 3.96$, the values are 3.62, 0.73, and 1.26, respectively. It is clear that forward scattering dominates at this value of x.

For $x = 1.84$, the total multiple scattered pressure can be estimated from Eq. (A4). Since the sand grains in Jansen's[9] experiments were confined in a 3-cm-wide rectangular tube, the ranges of $\delta + \rho$ and Φ in this case are the same as in Eqs. (A5) and (A6), but the range of ρ is limited to $r^* \leqslant \rho \leqslant r_{sj} + \lambda/4$, where r^* is the distance from the cylinder to the receiver (see Fig. A4). It can be seen that r^* changes with β. For simplicity, considering the narrow beam case, we assume r^* is constant and equal to 12 cm in Jansen's[9] experiments. The multiple scattered pressure then takes the form

$$P_{1j}/p_{sj} = 3k_c f_\infty M(r_0 - r^*)/2\rho_0' x^2. \qquad \text{(A21)}$$

For $M = 25.5$ kg/m^3, $\rho_0' = 2.65 \times 10^3$ kg/m^3, and $|f_\infty| = 0.7$, we obtain $|P_{1j}/p_{sj}| \approx 3.0$. For a single particle in the detected volume, the total scattered pressure at the receiving transducer is $p_{sj} + P_{ij}$. Ignoring phase differences between the scattered and rescattered waves, the total scattered pressure becomes

$$(1 + |P_{1j}/p_{sj}|)\hat{p}_s,$$

which at this concentration is about $4.0\,\hat{p}_s$, where $\hat{p}_s$ is the mean scattered pressure without multiple scattering. From Fig. A2(b), we find graphically that the actual scattered pressure at this concentration is $1.9\,\hat{p}_s$. The approximate predicted correction is therefore within a factor of 2 of that observed.

For $x = 3.96$, we consider forward multiple scattering only. In this case, the multiple scattered pressure can be estimated using Eq. (A18), but with r^* for the upper limit of δ. Working out the algebra, we obtain

$$\frac{P_{1j}}{p_{sj}} = \frac{af_\infty(0)N^{1/3}}{2} \ln\left(\frac{r_0 - r^*}{r^*} r_0 N^{1/3}\right). \qquad \text{(A22)}$$

For $M = 20.5$ kg/m^3, $\rho_0' = 2.65 \times 10^3$ kg/m^3, and $|f_\infty(0)| = 3.62$, we obtain $|P_{1j}/p_{sj}| \approx 0.8$. Again, the scattered pressure at the receiving transducer due to a single particle is $p_{sj} + P_{1j}$, but in this case it is possible to include the effects of the phase difference between the incident scattered wave and the forward rescattered wave. The phase difference between the forward scattered wave and the incident wave is $\pi/2$ (see Ref. 12). The total scattered pressure is therefore given approximately by

$$(1 + |P_{1j}/p_{ij}|^2)^{1/2}\hat{p}_s = \sqrt{1 + 0.8^2}\hat{p}_s = 1.3\,\hat{p}_s.$$

From Fig. A2(b), the actual scattered pressure at this concentration is seen to be $1.2\,\hat{p}_s$. The agreement between the predicted and actual total scattered pressures is good.

Now consider the apparent absence of multiple scattering effects in Schaafsma and der Kinderen's[7] results (Fig. A3). Since the maximum values of x in Schaafsma and der Kinderen's[7] experiments are less than 2.0, the isotropic scattering assumption is made. The multiple scattered pressure can be estimated using Eq. (A9), which is $|P_{1j}/p_{sj}| \approx (1.5 \sim 4.5)$ for $r_0 = 15$ cm and $|P_{1j}/p_{sj}| \approx (0.8 \sim 2.2)$ for $r_0 = 7.5$ cm at $M = 5$ kg/m^3. Again, ignoring phase differences due to scattering, the total scattered pressure is about $(2.5 \sim 5.5)\,\hat{p}_s$ for $r_0 = 15$ cm and $(1.8 \sim 3.2)\,\hat{p}_s$ for $r_0 = 7.5$ cm. The predicted values are such that multiple scattering effects would be expected in the data, but they are not observed, except perhaps for $a = 75\,\mu$m in Fig. A3(a). These measurements differ fundamentally from Jansen's,[9] however, in that the suspension was distributed along the entire acoustic path. The discrepancy may therefore be due to the fact that the phase differences between the scattered and rescattered waves, the transducer directivity, and the scattered pressure from particles in the other Fresnel zones have all been ignored. The estimates are more sensitive to these effects when the suspension fills the half-space viewed by the bistatic system and would tend to reduce the estimate of total scattered pressure.

From the above discussion, it can be seen that the nonlinear dependence of the attenuation coefficient on M at high concentrations could be due to multiple scattering, and the approximate correction for cases in which forward scattering dominates ($x \gg 1$) is in reasonable agreement with Jansen's[9] data. At smaller values of x, consistency with experiment is possible only if the scatterers are restricted to the transducer farfield; and even then, the predicted effects are too large. A more complete approach seems to be needed in this case. The most important conclusion as far as this article is concerned is that the data do not exhibit multiple scattering effects below concentrations of 10 kg m^{-3}. Measurements at larger concentrations were not used in the comparisons presented here.

[1]R. S. Dietz, "Deep Scattering layer in the Pacific and Antarctic Oceans," J. Mar. Res. **7**, 430–442 (1948).
[2]J. R. Proni, F.C. Newman, D. C. Rona, D. E. Drake, G. A. Berberian, C. A. Lauter, and R. L. Sellers, "On the Acoustics for Studying Suspended Oceanic Sediment and for Determining the Onset of the Shallow Thermocline," Deep-Sea Res. **23**, 831–837 (1976).
[3]M. H. Orr and F. R. Hess, "Remote Acoustic Monitoring of Natural Suspensate Distributions, Active Suspensate Resuspension, and Slope/Shelf Water Intrusions," J. Geophys. Res. **83**, 4062–4068 (1978).
[4]R. A. Young, J. T. Merrill, T. L. Clarke, and J. R. Proni, "Acoustic Profiling of Suspended Sediments in the Marine Bottom Boundary Layer," Geophys. Res. Lett. **9**, 175–178 (1982).
[5]A. E. Hay, "On the Remote Acoustic Detection of Suspended Sediment at Long Wavelengths," J. Geophys. Res. **88**(c12), 7525–7542 (1983).
[6]Y. Ma, V. K. Varadan, V. V. Varadan, and K. W. Bedford, "Multifrequency Remote Acoustic Sensing of Suspended Materials in Water," J. Acoust. Soc. Am. **74**, 581–585 (1983).
[7]A. S. Schaafsma and W. J. G. J. der Kinderen, "Ultrasonic Instruments for the Continuous Measurement of Suspended Sand Transport," in *Proceedings of the IAHR Symposium on Measuring Techniques in Hydraulic Research*, edited by A. C. E. Wessels (Balkema, Rotterdam, Delft, The Netherlands, 1986).
[8]G. H. Flammer, "Ultrasonic Measurement of Suspended Sediment," Geo. Survey Bull. No. 1141-A (US GPO, Washington, DC, 1962).
[9]R. H. Jansen, "An Ultrasonic Doppler Scatterometer for Measuring Suspended Sand Transport," in *Ultrasonic International 79, Conference Proceedings*, edited by Z. Novak (Graz, Austria, 1979), UI 79, pp. 366–369.
[10]T. L. Clarke, J. R. Proni, and J. F. Craynock, "A Simple Model for the Acoustic Cross Section of Sand Grains," J. Acoust. Soc. Am. **76**, 1580–1582 (1984).
[11]R. K. Johnson, "Sound Scattering From a Fluid Sphere Revisited," J. Acoust. Soc. Am. **61**, 375–377 (1977).
[12]J. Y. Sheng, *Sound Scattering and Attenuation in Aqueous Suspensions of Sand: Comparison of Theory and Experiment*, M.Sc. thesis (Memorial Univ. of Newfoundland, St. John's, Newfoundland, 1986).
[13]V. K. Varadan, Y. Ma, and V. A.Varadan, "A Multiple Scattering Theory for Elastic Wave Propagation in Discrete Random Media," J. Acoust. Soc. Am. **77**, 375–385 (1985).
[14]J. J. Faran, Jr., "Sound Scattering by Solid Cylinders and Spheres," J. Acoust. Soc. Am. **23**, 405–418 (1951).
[15]P. M. Morse and K. U. Ingard, *Theoretical Acoustics* (McGraw-Hill, New York, 1968).
[16]A. E. Hay and D. G. Mercer, "On the Theory of Sound Scattering and Viscous Absorption in Aqueous Suspensions at Medium and Short Wavelengths," J. Acoust. Soc. Am. **78**, 1761–1771 (1985).
[17]J. Y. Sheng and A. E. Hay, "Sound Scattering in Aqueous Suspensions of Sand: Comparison of Theory and Experiment," in *Progress in Underwater Acoustics*, edited by H. M. Merklinger (Plenum, New York, 1987), pp. 161–168.
[18]L. Flax, L. R. Dragonette, and H. Uberall, "Theory of Elastic Resonance Excitation by Sound Scattering," J. Acoust. Soc. Am. **63**, 723–731 (1978).
[19]J. A. Reagan and B. M. Herman, "Light Scattering by Irregularly Shaped Particles Versus Spheres: What are Some of the Problems Presented in Remote Sensing of Atmospheric Aerosols?," in *Light Scattering by Irregularly Shaped Particles*, edited by D. W. Schuerman (Plenum, New York, 1980), pp. 319–324.
[20]P. C. Waterman and R. Truell, "Multiple Scattering of Waves," J. Math. Phys. **2**, 512–538 (1961).
[21]T. M. Reed and K. E. Gubbins, *Applied Statistical Mechanics* (McGraw-Hill, New York, 1973), pp. 458–459.
[22]R. J. Urick, "The Absorption of Sound in Suspensions of Irregular Particles," J. Acoust. Soc. Am. **20**, 283–289 (1948).
[23]Y. Ma, V. K. Varadan, and V. V. Varadan, "Application of Twersky's Multiple Scattering Formalism to a Density Suspension of Elastic Particles in Water," J. Acoust. Soc. Am. **75**, 335–339 (1984).
[24]R. H. J. Jansen, "The *in-situ* Measurement of Sediment Transport by Means of Ultrasound Scattering," Report 203, Delft Hydraulics Laboratory, Delft, The Netherlands, 1978.